

Winding Clearness for Differentiable Point Cloud Optimization

DONG XIAO, Tsinghua University, China and Beijing National Research Center for Information Science and Technology, China

YUEJI MA, Tsinghua University, China

ZUOQIANG SHI*, Tsinghua University, China and Yanqi Lake Beijing Institute of Mathematical Sciences and Applications, China

SHIQING XIN, Shandong University, China

WENPING WANG, Texas A&M University, USA

BAILIN DENG, Cardiff University, UK

BIN WANG*, Tsinghua University, China and Beijing National Research Center for Information Science and Technology, China

We propose to explore the properties of raw point clouds through the *winding clearness*, a concept we first introduce for assessing the clarity of the interior/exterior relationships represented by the winding number field of the point cloud. In geometric modeling, the winding number is a powerful tool for distinguishing the interior and exterior of a given surface $\partial\Omega$, and it has been previously used for point normal orientation and surface reconstruction. In this work, we introduce a novel approach to assess and optimize the quality of point clouds based on the winding clearness. We observe that point clouds with reduced noise tend to exhibit improved winding clearness. Accordingly, we propose an objective function that quantifies the error in winding clearness, solely utilizing the positions of the point clouds. Moreover, we demonstrate that the winding clearness error is differentiable and can serve as a loss function in optimization-based and learning-based point cloud processing. In the optimization-based method, the loss function is directly back-propagated to update the point positions, resulting in an overall improvement of the point cloud. In the learning-based method, we incorporate the winding clearness as a geometric constraint in the diffusion-based 3D generative model. Experimental results demonstrate the effectiveness of optimizing the winding clearness in enhancing the quality of the point clouds. Our method exhibits superior performance in handling noisy point clouds with thin structures, highlighting the benefits of the global perspective enabled by the winding number.

Additional Key Words and Phrases: Geometric modeling, Winding number, Point cloud denoising, Diffusion model

1 INTRODUCTION

The winding number serves as a valuable tool for determining the inside/outside position of a query point $\mathbf{q} \in \mathbb{R}^3$ relative to a given closed surface $\partial\Omega$. This tool has found widespread application in various geometric tasks [Jacobson et al. 2013; Wang et al. 2022a,b]. In recent years, there has

been a growing research effort into its applicability for point cloud processing. Existing studies mainly focus on leveraging the winding number theory for normal orientation and surface reconstruction from point clouds [Lin et al. 2023; Lu et al. 2019; Metzner et al. 2021; Xu et al. 2023].

In this paper, we investigate a new application of the winding number in evaluating and enhancing the quality of point clouds using the winding number theory. Point clouds frequently suffer from issues such as noise, as documented in [Berger et al. 2017], which can compromise their geometric representation quality and accuracy. The need to improve the quality of point clouds is evident in various scenarios. For instance, in the realm of 3D deep learning, the 3D diffusion model has been widely applied to point cloud generation tasks [Luo and Hu 2021; Zeng et al. 2022; Zhou et al. 2021]. However, the ongoing potential for improving the quality of the generated point sets is substantial. The datasets utilized for 3D generation typically feature thin structures. Many traditional denoising methods utilize the nearest neighbors of a point to model its local neighborhood on the underlying surface and analyze its geometric properties. However, such a local approach may fail on thin structures, as the nearest neighbors may include points from the other side of the surface that do not belong to the local neighborhood. In this work, we leverage the global awareness of the winding number to offer a fresh perspective on these problems.

Our main observation is that a high-quality point cloud, for instance, with a low noise level, tends to exhibit improved clarity in the internal/external relationship determined by the winding number field, demonstrating better *winding clearness*. Specifically, the winding number value of the sample points approaches the iso-value $1/2$. Meanwhile, the value in the bounding box, slightly larger than the shape, approaches zero. We define the difference between the actual values and the expected values of the winding number field at these specific points as the *winding clearness error*. The point clouds with less noise typically display lower winding clearness errors.

Additionally, as the winding clearness error is a differentiable function that solely depends on the point positions of the point cloud, we can treat it as a loss function for point cloud optimization and integrate it into processing pipelines that require differentiability. In this paper, we demonstrate its applicability in both optimization-based and learning-based methods. In the former case, the loss function is directly back-propagated to optimize point positions without employing a neural network. In the latter case, we incorporate winding clearness as a geometric constraint and integrate it with diffusion-based 3D point cloud generation, allowing us to fine-tune the generative model and improve the quality of the resulting point clouds.

In the experiments, we demonstrate that improving the winding clearness using both optimization and learning-based methods enhances the quality of the point cloud. We conduct experiments on various datasets and compare our methods with related approaches. The results indicate that our method

*Corresponding authors

Authors' addresses: Dong Xiao, xiaod18@mails.tsinghua.edu.cn, Tsinghua University, China; Beijing National Research Center for Information Science and Technology, China; Yueji Ma, myj21@mails.tsinghua.edu.cn, Tsinghua University, China; Zuoqiang Shi, zqshi@tsinghua.edu.cn, Tsinghua University, China; Yanqi Lake Beijing Institute of Mathematical Sciences and Applications, China; Shiqing Xin, xinshiqing@sdu.edu.cn, Shandong University, China; Wenping Wang, wenping@tamu.edu, Texas A&M University, USA; Bailin Deng, DengB3@cardiff.ac.uk, Cardiff University, UK; Bin Wang, wangbins@tsinghua.edu.cn, Tsinghua University, China; Beijing National Research Center for Information Science and Technology, China.

exhibits competitive performance on traditional geometric models. Moreover, our method demonstrates superior performance in handling noisy point clouds with thin structures, surpassing traditional methods that rely on local neighborhood information. This finding underscores the effectiveness of the global perspective brought by the winding number.

2 RELATED WORK

In this section, we provide a review of relevant studies into three aspects: the utilization of the winding number in point cloud processing, the management of low quality point clouds, and the generation of 3D point clouds utilizing the diffusion-based technique.

2.1 Winding Number for Geometry Processing of Point Clouds

The winding number has proven to be a valuable tool in 3D geometry processing, as demonstrated in previous studies [Barill et al. 2018; Jacobson et al. 2013]. This concept can also be understood by the Gauss Lemma in potential energy theory [Lin et al. 2023; Lu et al. 2019; Wendland 2009] or the electronic dipole field [Metzger et al. 2021]. Although this concept is commonly utilized in mesh processing tasks, such as boolean operations [Zhou et al. 2016] and medial axis transform [Wang et al. 2022a], our focus is on investigating the application of the winding number theory to point processing problems, especially after discretizing the surface integral.

Approaches such as fast winding [Barill et al. 2018] and GR [Lu et al. 2019] leverage the winding number for various point cloud tasks, including the oriented surface reconstruction. They also utilize the fast multipole method (FMM) [Greengard and Rokhlin 1987] to enhance the computational efficiency. PGR [Lin et al. 2023] introduces an innovative approach that eliminates the reliance on surface normals and achieves unoriented surface reconstruction by treating the surfels as unknowns and solving a linear equation to determine the magnitude and direction of the surfels. GCNO [Xu et al. 2023] addresses the challenge of globally consistent normal orientation by regularizing the winding number field with a series of constraints. The point positions in the aforementioned methods remain static. By contrast, our approach offers a fresh perspective by integrating the winding number into new geometric problems. We improve the quality of the point clouds by adjusting point positions to achieve enhanced winding clearness.

2.2 Management of Low Quality Point Clouds

Point clouds are commonly used data structures for representing geometric shapes, but they frequently suffer from artifacts such as noise [Berger et al. 2017]. Denoising is a widely explored approach to address this issue and improve the quality of point clouds. This problem has been extensively studied for several decades, as reviewed in [Han et al. 2017] and [Zhou et al. 2022]. Numerous traditional denoising methods, such as bilateral smoothing [Digne and de Franchis 2017; Zhang et al. 2019] and jet smoothing [Cazals and Pouget 2005], mainly focus on local filtering and rely on the nearest neighbor computation. LOP [Lipman et al. 2007] and WLOP [Huang et al. 2009] utilize the local projection strategy and iteratively refine a point cloud subset, which acts as a denoised representation of the original point set. The above-mentioned methods frequently face challenges when dealing with thin structures. There are other denoising methods based on different mechanism, for instance, Moving Least Squares (MLS) surfaces [Guennebaud and Gross 2007; Öztireli et al. 2009], L_1 and L_0 regularization [Avron et al. 2010; Sun et al. 2015], Taubin smoothing [Agathos et al. 2022], low rank optimization [Lu et al. 2022] or deep neural networks [Agathos et al. 2022; Rakotosaona et al. 2020; Zhang et al. 2021]. However, the capacity of global awareness in previous methods of addressing this issue remains limited.

2.3 Diffusion-based 3D Generation of Point Clouds

Notable advancements in diffusion-based point cloud generation have emerged in recent years due to the increasing popularity of 3D generative models, specifically the Denoising Diffusion Probabilistic Models (DDPM) [Ho et al. 2020a]. The diffusion model involves learning a probabilistic denoising procedure, encompassing a reverse process and a generative process. DPM [Luo and Hu 2021] models the reverse process as a Markov chain operating on the latent space of shapes. PVD [Zhou et al. 2021] utilizes a point-based network as a foundation for generating point clouds from an initial Gaussian prior with the same dimension as the result. LION [Zeng et al. 2022], proposed by NVIDIA, introduces a hierarchical generation process that combines the global shape latent with the point-structured latent. However, prior research in this domain predominantly focuses on ensuring the similarity between the generated point sets and the original dataset, with limited specific consideration for the quality of the generated point clouds. To fill this gap, we propose the incorporation of a differentiable point cloud optimization technique for this problem.

3 PRELIMINARIES: WINDING NUMBER AND ITS APPLICATION IN SURFACE RECONSTRUCTION

3.1 Inside/Outside Determination and Surface Reconstruction

The primary purpose of the winding number is to ascertain the spatial relationship between a given query point $\mathbf{x} \in \mathbb{R}^3$ and a specified surface $\partial\Omega$. When Ω is an open and bounded set with a smooth boundary in \mathbb{R}^3 , the winding number is defined as a surface integral of $\partial\Omega$ with respect to the point \mathbf{x} :

$$\chi(\mathbf{x}) = \int_{\partial\Omega} K(\mathbf{x}, \mathbf{y}) \cdot \vec{N}(\mathbf{y}) \, dS(\mathbf{y}), \quad K(\mathbf{x}, \mathbf{y}) = -\frac{(\mathbf{x} - \mathbf{y})}{4\pi\|\mathbf{x} - \mathbf{y}\|^3}. \quad (1)$$

Here, $\vec{N}(\mathbf{y})$ represents the outward unit normal vector at point \mathbf{y} , and $dS(\mathbf{y})$ denotes the surface element. The $K(\mathbf{x}, \mathbf{y})$ is a vector-valued function with a range dimension of 3. It is the gradient of the fundamental solution of the 3D Laplace equation.

The resulting value of the integral $\chi(\mathbf{x})$ serves as the indicator function of the surface $\partial\Omega$, representing whether the query point \mathbf{x} lies inside, outside, or on the surface:

$$\chi(\mathbf{x}) = \begin{cases} 0 & \mathbf{x} \in \mathbb{R}^3 \setminus \overline{\Omega} \\ 1/2 & \mathbf{x} \in \partial\Omega \\ 1 & \mathbf{x} \in \Omega. \end{cases} \quad (2)$$

Once the indicator function for a closed surface in the ambient space is determined using Equation (1), the surface can be reconstructed by extracting the iso-surface with a value of 1/2. Techniques such as GR [Lu et al. 2019] and fast winding [Barill et al. 2018] utilize the discrete form of Equation (1) for surface reconstruction from oriented point clouds. In these methods, the indicator function of the input is computed directly using the following discrete winding number formulation:

$$\chi(\mathbf{x}) = \sum_{i=1}^N K(\mathbf{x}, \mathbf{y}_i) \cdot \mu_i, \quad \mu_i = a_i \mathbf{n}_i, \quad (3)$$

where \mathbf{n}_i is the outward unit normal of the point \mathbf{y}_i , a_i is the discrete surface element computed using the geodesic Voronoi area associated with \mathbf{y}_i . μ_i is a 3-dimensional vector and can be understood as the surfels mentioned in [Pfister et al. 2000].

It is important to note that the integrand becomes singular as \mathbf{x} approximates \mathbf{y}_i . This situation should be carefully considered, particularly when \mathbf{x} approaches the surface. Consequently, GR [Lu et al. 2019] modifies the

integrand of Equation (3) as follows:

$$\tilde{K}(\mathbf{x}, \mathbf{y}_i) = \begin{cases} -\frac{(\mathbf{x} - \mathbf{y}_i)}{4\pi\|\mathbf{x} - \mathbf{y}_i\|^3} & \|\mathbf{x} - \mathbf{y}_i\| \geq w(\mathbf{x}) \\ -\frac{(\mathbf{x} - \mathbf{y}_i)}{4\pi w(\mathbf{x})^3} & \|\mathbf{x} - \mathbf{y}_i\| < w(\mathbf{x}). \end{cases} \quad (4)$$

In this modification, the width coefficient $w(\mathbf{x})$ is determined by a specific formulation outlined in GR. The use of the new kernel function \tilde{K} significantly enhances the algorithm performance for surface reconstruction. In the experimental section, we maintain a fixed value of $w(\mathbf{x})$ as 0.04.

3.2 Surface Reconstruction for Unoriented Point Sets

The reconstruction algorithm described in the previous section for GR requires consistently oriented normals as inputs. The reason is that the winding number formula relies on these normals to determine the spatial relationship. A recent approach PGR [Lin et al. 2023] eliminates the need for normals by treating the surfels μ_i in Equation (3) as unknowns and solves a linear equation system based on the on-surface constraints – the point cloud is sampled from the surface, indicating that the winding number should equal to $1/2$ at all the sample points $P = \{\mathbf{p}_1, \mathbf{p}_2, \dots, \mathbf{p}_N\}$ according to Equation (2). Here, N denotes the number of points. This observation leads to N equations:

$$\chi(\mathbf{p}_j) = \frac{1}{2}, \quad j = 1, 2, \dots, N. \quad (5)$$

We can derive the following set of linear equations by combining Equations (3), (4), and (5):

$$\sum_{i=1}^N \tilde{K}(\mathbf{p}_j, \mathbf{p}_i) \cdot \mu_i = \frac{1}{2}, \quad j = 1, 2, \dots, N. \quad (6)$$

Each μ_i is a 3-dimensional vector with $\mu_i = (\mu_{i1}, \mu_{i2}, \mu_{i3})^T$. These equations can be expressed in matrix form as follows:

$$A(P)\mu = b, \quad (7)$$

where $\mu = (\mu_{11}, \mu_{12}, \mu_{13}, \dots, \mu_{N3})^T$, $b = \frac{1}{2}\mathbf{1}$ is a vector where all elements are $1/2$, and $A(P)$ is a $N \times 3N$ matrix with

$$[A(P)]_{j,3i+k} = [\tilde{K}(\mathbf{p}_j, \mathbf{p}_i)]_k. \quad (8)$$

The matrix $A(P)$ is solely dependent on the sample points $P = \{\mathbf{p}_1, \mathbf{p}_2, \dots, \mathbf{p}_N\}$. In PGR, this set of linear equations is transformed into a linear least squares problem. It is worth noting that this problem is underdetermined, with N equations and $3N$ unknowns. Moreover, the matrix $A^T A$ typically has a large condition number. PGR introduces a regularization term $R(P)$ to alleviate this issue. The resulting optimization problem is:

$$\min_{\mu} \frac{1}{N} (\|A(P)\mu - b\|^2 + \alpha\mu^T R(P)\mu), \quad (9)$$

with

$$R(P) = \text{diag}(A(P)^T A(P)). \quad (10)$$

Here, “diag” represents a matrix that retains only its diagonal elements. The parameter α is user-specific, and we set it to 0.5 in the experimental section. By solving this optimization problem, we can obtain the surfels μ with globally consistent orientations, thereby allowing us to reconstruct the surface using the GR method in Section 3.1.

4 WINDING CLEARNESS

In this section, we aim to expand the applicability of the winding number theory to a broader range of point geometry problems. The algorithm discussed in the preceding section is chiefly focused on optimizing the surfels to ensure that the winding number field closely approximates $1/2$ at the sampling points. Intuitively, a high-quality point cloud, such as one with minimal noise, typically displays clear internal and external relationships in the resulting winding number field, as depicted in Fig. 1. Consequently, the

optimal value of Equation (9) will be small in this case. Hence, we introduce the concept of *winding clearness*, which represents the difference between the actual values and the expected values of the winding number field at specific points. Our observations also indicate that the winding number should equal to zero outside the surface. In addition to using the value of Equation (9) as the measure of the winding clearness, we establish a bounding box larger than the original object and sample $2N$ points $Q = \{\mathbf{q}_1, \mathbf{q}_2, \dots, \mathbf{q}_{2N}\}$ on this box by trimesh [Dawson-Haggerty et al. 2021]. These boundary points are predetermined and remain unchanged throughout the optimization. The expected indicator function values for these $2N$ points should be zero:

$$\chi(\mathbf{q}_j) = 0, \quad j = 1, \dots, 2N. \quad (11)$$

These supplementary constraints lead to:

$$A_2(P)\mu = \vec{0}, \quad [A_2(P)]_{j,3i+k} = [\tilde{K}(\mathbf{q}_j, \mathbf{p}_i)]_k. \quad (12)$$

The boundary points Q will not be optimized during the algorithm in the next section. Accordingly, we do not express Q as the variables. By combining Equations (5) and (11), and denoting $A(P)$ in Equation (7) as $A_1(P)$, we can express the modified objective function as follows:

$$\min_{\mu} f(P, \mu), \quad (13)$$

where

$$f(P, \mu) = \frac{1}{N} (\|A_1(P)\mu - b\|^2 + \frac{\eta}{2} \|A_2(P)\mu\|^2 + \alpha\mu^T R(P)\mu). \quad (14)$$

η is a user specific parameter to control the contribution of the bounding box constraint. The expression for the regularization term $R(P)$ is modified as follows:

$$R(P) = \text{diag}(A_1(P)^T A_1(P) + \frac{\eta}{2} A_2(P)^T A_2(P)). \quad (15)$$

The minimization problem of Equation (13) can be solved by $\nabla_{\mu} f(P, \mu) = 0$, which leads to

$$\mu(P) = (A_1(P)^T A_1(P) + \frac{\eta}{2} A_2(P)^T A_2(P) + \alpha R(P))^{-1} (A_1(P)^T b). \quad (16)$$

Notably, $\mu(P)$ only depends on the point positions P . Moreover, as A_1, A_2, R are all smooth functions of P and matrix inversion is differentiable, the function $\mu(P)$ defined in Equation (16) is a differentiable function of P . The winding clearness error $W(P)$ is then defined as the minimum value of f :

$$W(P) = f(P, \mu(P)) = \frac{1}{N} (b^T b - b^T A_1(P)\mu(P)), \quad (17)$$

which is also a differentiable function of P . This important property enables us to employ winding clearness in point cloud processing pipelines that require differentiability, including both optimization-based and learning-based methods. This will be discussed in detail in Section 5.

A lower value of the function $W(P)$ signifies a better winding clearness. In Table 1, we present the winding clearness error for point clouds of a 2D circle composed of 1000 points with a radius of 0.5. We add randomized Gaussian noise with varying standard deviations σ ranging from 0 to 0.05 to the point cloud. The bounding box Q is defined as a cubic region with the coordinate range as $[-0.7, 0.7]$ and η is set to 50.0 for robustness against various levels of noise. In the 2D scenario, the winding number theory remains relevant. However, the integrand should be replaced with the directional derivative of the fundamental solution of the 2D Laplace equation rather than the 3D counterpart. The results indicate that the winding clearness error increases as the noise level increases. Fig. 1 showcases the winding number field generated by varying noise standard deviations, along with the annotation of the winding clearness error (WCE) and its constituent values. In the case of point clouds with substantial noise, achieving surfels that bring the winding number field of all the sampling points in case proximity to $1/2$ becomes increasingly challenging. Although the surfels solved in high noise conditions can result in a considerable number of points approaching $1/2$,

Table 1. The winding clearness error (WCE) of a circle composed of 1000 points with a radius of 0.5. We add randomized Gaussian noise with varying standard deviations σ ranging from 0 to 0.05. The WCE value is multiplied by 10^3 .

σ	0	0.001	0.002	0.005	0.01	0.02	0.05
WCE	2.59	3.29	4.41	8.30	8.94	9.62	11.86

as illustrated in $\sigma = 0.05$ of Fig. 1, the surfels become large in this case, resulting in a substantial increase in the regularization term $\mu^T R(P)\mu$.

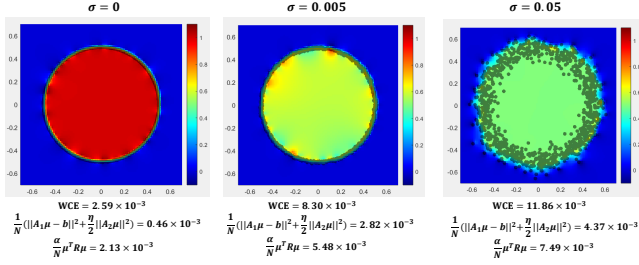


Fig. 1. Winding number field formed by 2D circles within noise of different standard deviations. We annotate the winding clearness error (WCE) and the values of its constituents. The black dots represent the sample points.

5 OPTIMIZATION OF THE WINDING CLEARNESS

The winding clearness error $W(P)$ can be calculated for a raw point cloud P using Equations (17) and (16). It is reasonable to assume that improving the winding clearness, indicated by reducing the value of $W(P)$, will have a positive influence on the overall quality of the point cloud. The computation of $W(P)$ is fully differentiable because it mainly involves linear algebraic operations. Consequently, we propose to utilize $W(P)$ as the loss function for point cloud optimization. The value of $W(P)$ can be directly back-propagated to the point positions, which holds the potential to enhance the quality of the point cloud by reducing the noise. In this regard, we present both an optimization-based approach (Section 5.1) and a learning-based approach (Section 5.2) for optimizing the winding clearness of raw point clouds.

5.1 Optimization-based Method

The optimization-based method does not rely on the deep neural network. Instead, we utilize a gradient-based optimization approach to optimize the winding clearness of the given point set directly. To ensure that the resulting point cloud does not deviate excessively from the original one (denoted as P_0), we incorporate an L_2 regularization term to penalize the distance between the results and the original point clouds. The loss function is defined as follows:

$$\text{Loss}(P) = W(P) + \frac{\lambda}{N} \|P - P_0\|^2, \quad (18)$$

where λ is a user specific parameter and N represents the number of points. We utilize the gradient-based Adam optimizer [Kingma and Ba 2015] in PyTorch [Paszke et al. 2019] for back-propagation. The calculation of $W(P)$ involves obtaining $\mu(P)$ by computing an inverse matrix as Equation (16). To ensure differentiability, we perform this operation by solving a linear system using the PyTorch function `torch.linalg.solve`, which is a numerically stable solver with the back-propagation mechanism. Specifically, the computation

of $\mu(P)$ is performed as follows:

$$\tilde{A} = A_1(P)^T A_1(P) + \frac{\eta}{2} A_2(P)^T A_2(P) + \alpha R(P), \quad (19)$$

$$\tilde{b} = A_1(P)^T b, \quad (20)$$

$$\mu = \text{torch.linalg.solve}(\tilde{A}, \tilde{b}). \quad (21)$$

Subsequently, the calculation of $W(P)$ involves inserting $\mu(P)$ to $f(P, \mu)$ in Equation (14). The derivative $dW(P)/dP$ can then be computed utilizing the chain rule and back-propagation of PyTorch. The loss function directly facilitates the adjustment of the point positions, resulting in enhanced winding clearness. The learning rate of the Adam optimizer is set to $1e^{-3}$.

Fig. 2 depicts a 2D example with a thin structure to demonstrate the effectiveness of our method. The input consists of 1000 points sampled from an elongated rectangle with a long axis of 1.0 and a short axis of 0.02. Thereafter, per-point Gaussian noise of the standard deviation 0.004 is added to the point set. We optimize the point positions through Equation (18). After 100 Adam iterations, the resulting point cloud exhibits reduced noise, and the rectangle structure is preserved, highlighting the capability of our method in addressing noisy thin structures.

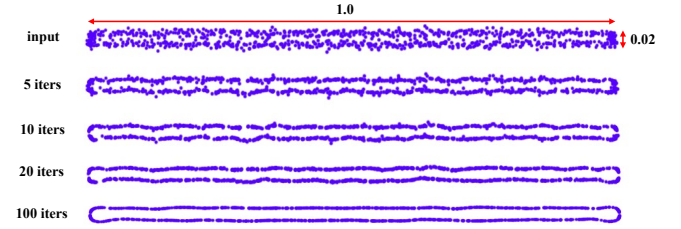


Fig. 2. Iterative process of our method applied to a noisy point cloud of a thin rectangle.

The matrix \tilde{A} in Equation (19) may be singular theoretically. This issue can be addressed using the pseudo-inverse when the determinant of \tilde{A} is zero in this step, which is also differentiable in PyTorch. However, the singular matrices constitute a set of measure zero within the set of all matrices. Additionally, the incorporation of the regularization term $R(P)$ further decreases the likelihood of encountering the non-invertible scenario during the optimization. To date, our optimization process has not encountered situations where the matrix is completely non-invertible numerically.

5.2 Learning-based Method

In addition to optimizing the point cloud directly using Equation (18), the winding clearness error $W(P)$ can also be considered as a geometric constraint and applied in various learning-based point processing tasks. In this section, we propose to incorporate this consideration with the diffusion-based 3D generative model. The Denoising Diffusion Probabilistic Model (DDPM) [Ho et al. 2020b] has gained significant popularity and is utilized in various 3D point cloud generation tasks [Luo and Hu 2021; Zeng et al. 2022; Zhou et al. 2021]. The current loss functions of these methods primarily focus on ensuring the similarity between the generated data and the original dataset, but lack a specific term for constraining the geometric properties. Our method provides a solution for this gap by optimizing the winding clearness of the generated results within a joint training strategy.

We adopt the PVD [Zhou et al. 2021] as our baseline method, which adheres to a standard DDPM process and exhibits competitive performance in unconditional point cloud generation. The diffusion model involves two steps: a noise adding process $q(\mathbf{x}_{0:T})$ and a denoising process $p_\theta(\mathbf{x}_{0:T})$.

performed over T steps:

$$q(\mathbf{x}_{0:T}) = q(\mathbf{x}_0) \prod_{t=1}^T q(\mathbf{x}_t | \mathbf{x}_{t-1}), \quad (22)$$

$$p_\theta(\mathbf{x}_{0:T}) = p(\mathbf{x}_T) \prod_{t=1}^T p_\theta(\mathbf{x}_{t-1} | \mathbf{x}_t), \quad (23)$$

where $q(\mathbf{x}_0)$ signifies the data distribution, and $p(\mathbf{x}_T)$ denotes an initial Gaussian prior. The sequence $\mathbf{x}_T, \mathbf{x}_{T-1}, \dots, \mathbf{x}_0$ illustrates the denoising process within the diffusion model. θ corresponds to the network parameters. The Point-Voxel CNN [Liu et al. 2019] is chosen as the backbone network of PVD, specifically corresponding to ϵ_θ in Equation (25) below.

During the training process, PVD learns the marginal likelihood and maximizes the variational lower bound similar to traditional DDPM, which can be expressed as follows:

$$\max_{\theta} E_{q(\mathbf{x}_0)} [\log p_\theta(\mathbf{x}_0)]. \quad (24)$$

After reparameterization and rigorous mathematical deduction (as described in [Ho et al. 2020b] and [Zhou et al. 2021]), the training objective function is transformed to:

$$\min ||\epsilon - \epsilon_\theta(\mathbf{x}_t, t)||^2, \epsilon \sim \mathcal{N}(0, I). \quad (25)$$

The training process aims to make the values ϵ_θ approach a normal distribution for specific variables.

The test process of PVD involves generating a point cloud \mathbf{x}_0 from a randomly sampled initial Gaussian prior \mathbf{x}_T and a series of Gaussian noise \mathbf{z}_t . The generation process can be described as follows:

$$\mathbf{x}_{t-1} = \frac{1}{\sqrt{\alpha_t}} (\mathbf{x}_t - \frac{1 - \alpha_t}{\sqrt{1 - \alpha_t}} \epsilon_\theta(\mathbf{x}_t, t)) + \sqrt{\beta_t} \mathbf{z}_t \quad (26)$$

Here, all α_t , $\tilde{\alpha}_t$ and β_t values are specific or computed parameters in the DDPM, $\mathbf{z}_t \sim \mathcal{N}(0, I)$, and ϵ_θ is the same as Equation (25). This generation process can be represented as:

$$\mathbf{x}_0 = G(\mathbf{x}_t, \theta, \mathbf{z}, \alpha, \beta). \quad (27)$$

where \mathbf{z} represents all \mathbf{z}_t values, α denotes all α_t and $\tilde{\alpha}_t$ values, and β indicates all β_t values. Although we do not provide detailed explanations for all these parameters in our work due to space constraints, more contents about DDPM can be found in the references [Ho et al. 2020b] and [Zhou et al. 2021].

To incorporate winding clearness as the geometric constraint in the diffusion model, our approach utilizes a joint training strategy, which consists of a training branch and a generation branch. In the training branch, the loss function is the same as Equation (25). In the generation branch, a testing process described by Equation (27) is executed while maintaining the propagation of the gradients.

For the generation branch, we sample $\tilde{\mathbf{x}}_T$ from a Gaussian distribution and produce the output $\tilde{\mathbf{x}}_0$ using Equations (26) and (27). Wavy lines are used for distinction between the training and the generation branches. Subsequently, the winding clearness error of the generated point cloud $\tilde{\mathbf{x}}_0$ is added to the loss function as $W(\tilde{\mathbf{x}}_0)$. The total loss is then calculated as the combined sum of the losses from the training and generation branches. The joint training process is taking the gradient decent step as follows:

$$\nabla_{\theta} (||\epsilon - \epsilon_\theta(\mathbf{x}_t, t)||^2 + \rho W(\tilde{\mathbf{x}}_0)), \quad (28)$$

where the parameter ρ is user-specific and determines the balance between the training and generation branches.

Given that $W(\tilde{\mathbf{x}}_0)$ serves as a fine-tuning of the original model, the gradient of the generation branch is only propagated when $t < t_s$. Specifically, when $t \geq t_s$ (where t ranges from T to 0 in the denoising process), the gradients of the intermediate results $\tilde{\mathbf{x}}_t$ are detached in the computation

graph of PyTorch. Therefore, no gradients will be propagated beyond t_s . In the specific case of PVD, we set T to 1000 and t_s to 10 in our method.

The joint training strategy of Equation (28) can commence from a pre-trained model and act as a fine-tuning process for the original model. In the experimental section, we demonstrate that a certain duration of fine-tuning can significantly improve the quality of the generated point clouds.

6 EXPERIMENTS

The experimental section is organized as follows. In Section 6.1, we will showcase the influence of different noise scales on the winding clearness error of point clouds. Subsequently, we will illustrate the improvement in point cloud quality achieved through the optimization of the winding clearness. The results of the optimization-based method will be presented in Section 6.2. Meanwhile, the learning-based method will be presented in Section 6.3.

6.1 Winding Clearness Error of Noisy Inputs

In Section 4, we have demonstrated the winding clearness error of a 2D unit circle considering varying levels of Gaussian noise. Here, our attention turns toward the evaluation of 3D shapes. In Fig. 3(a), we display several frequently utilized shapes in computer graphics. Each shape is normalized to a maximum axis length of 1.0. We sample 5000 points from each shape using trimesh [Dawson-Haggerty et al. 2021]. Subsequently, we add randomized Gaussian noise of seven different amplitudes (0, 0.001, 0.002, 0.005, 0.01, 0.02, 0.05) to the clean point cloud, resulting in seven different scales of noisy point clouds for each shape. The calculation of the winding clearness error for each shape is performed utilizing Equations (17) and (16), with the bounding box Q set at -0.7 and 0.7 . η in Equation (14) is set to 200.0 for robustness against various levels of noise. Fig. 3(b) shows the winding clearness error of these shapes within different noise amplitudes, where we can observe a positive correlation between the winding clearness error and the noise magnitude. Therefore, we can expect that optimization of the winding clearness can help in minimizing the point cloud noise.

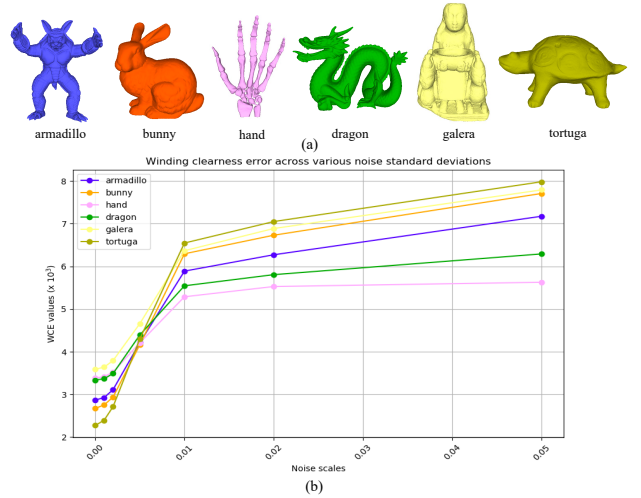


Fig. 3. Winding clearness error (WCE) of point clouds across various noise standard deviations σ sampled from several frequently utilized shapes. The WCE values are multiplied by 10^3 .

Table 2. Quantitative comparisons of the reconstructed mesh quality in the ordinary dataset. We show the Chamfer distance (CD) and the normal consistency (NC) of each method. The CD values are multiplied by 10^2 . Our method exhibits superior performance against local feature-based methods.

Model	WLOP		Bilateral		Jet		Ours	
	CD↓	NC↑	CD↓	NC↑	CD↓	NC↑	CD↓	NC↑
think10k298321	1.874	0.777	1.378	0.832	2.337	0.723	1.246	0.877
think10k314586	1.391	0.608	0.681	0.849	0.731	0.797	0.603	0.887
think10k73183	1.120	0.965	0.514	0.971	0.637	0.965	0.385	0.986
think10k39084	1.110	0.897	0.670	0.942	0.935	0.917	0.628	0.955
scissors4	1.490	0.505	0.786	0.766	0.767	0.742	0.623	0.827
wrench22	1.167	0.879	0.426	0.904	0.423	0.897	0.375	0.908
saxophone2	0.739	0.939	0.418	0.962	0.378	0.956	0.314	0.969
avg. of ordinary	1.098	0.868	1.078	0.884	1.066	0.874	0.921	0.897

6.2 Results of the Optimization-based Method

In this section, we validate the effectiveness of the optimization-based method proposed in Section 5.1. The loss function is defined as Equation (18), and we utilize 100 Adam iterations to enhance the winding clearness of each shape. Fig. 4 depicts the loss history of several shapes together with the reconstructed mesh of the input point cloud and the resulted point cloud of our method. Each input comprises 5000 sample points with Gaussian noise $\sigma = 0.005$. Although the computation of $W(P)$ involves an inverse matrix calculation, the loss function still converges smoothly and maintains a decreasing trend. The output point cloud also exhibits significant quality improvement.

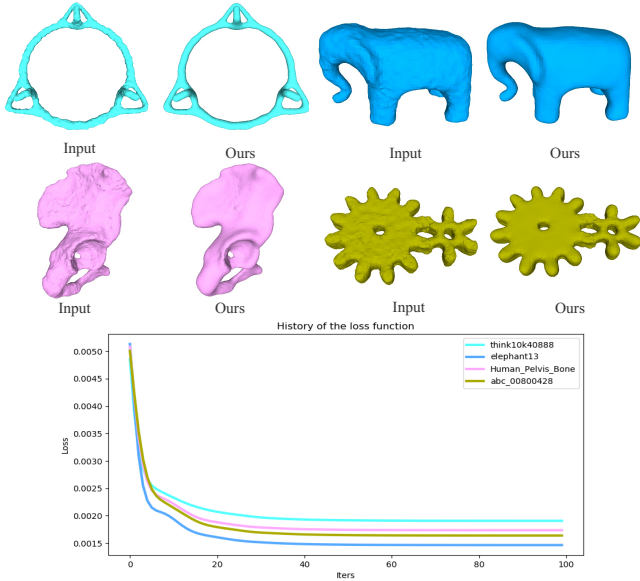


Fig. 4. Loss function history of several examples. The winding clearness can be effectively optimized, resulting in a marked enhancement in the quality of the output.

We conduct qualitative comparisons with relevant approaches to further validate the efficacy of our method. Herein, we will first evaluate the performance of our method on several commonly used geometric shapes. Subsequently, we will conduct experiments using a benchmark dataset compiled by a recent survey paper [Huang et al. 2022]. This dataset encompasses a comprehensive collection of shapes sourced from diverse repositories, such

as 3DNet [Wohlkinger et al. 2012], ABC [Koch et al. 2019], Thingi10K [Zhou and Jacobson 2016], and 3D Scans [Oliver, L. et al. 2012]. All the shapes of this benchmark are categorized based on the complexity for reconstruction. In our experiments, we specifically use the *ordinary* dataset, which consists of 486 shapes and offers a comprehensive evaluation of the robustness for each method. In particular, this dataset includes a significant proportion of shapes that exhibit thin structures.

We compare our method with several traditional point cloud filter approaches, including bilateral smoothing [Digne and de Franchis 2017], jet smoothing [Cazals and Pouget 2005] and WLOP [Huang et al. 2009]. Bilateral and jet smoothing are mainly based on nearest neighbor filtering. Meanwhile, WLOP achieves local optimal projection through an iterative process. We apply the CGAL [Fabri and Pion 2009] implementation of all these approaches. The bilateral implementation of CGAL also inherits the philosophy of EAR [Huang et al. 2013] as illustrated in the official documentation of CGAL. In WLOP, the parameter “representative particle number” is set to 95% of the original point set, and the parameter “neighbor radius” is set to 0.04. In jet smoothing, the sole parameter “neighbor size” is set as 15. In bilateral smoothing, the parameters “neighbor size”, “sharpness angle”, and “iters” are set to 10, 25, and 5, respectively. We utilize the reconstructed surface as a measure of the point cloud quality. An unoriented reconstruction method is necessary for this step. Instead of utilizing PGR [Lin et al. 2023] discussed in Section 3, we use iPSR [Hou et al. 2022] with point weight of 4.0 when comparing with these approaches. iPSR utilizes an iterative manner for normal updating. Therefore, the convergence performance of iPSR can effectively reflect the noise level in thin structures.

In Fig. 7, we present a qualitative comparison of several commonly utilized geometric shapes. The input datasets consist of 5000 points, with the first two rows exhibiting randomized Gaussian noise $\sigma = 0.005$ and the last two rows with $\sigma = 0.01$. The parameters η in Equation (14) is set to 10.0 and λ in Equation (18) is set to 20.0, and the bounding box is established at -0.6 and 0.6 , a range sufficient to encompass 3σ . In this figure, “iPSR” denotes the results reconstructed from the original noisy point clouds, while the subsequent columns showcase the reconstructed meshes of the corresponding denoising approaches. Our method demonstrates well-rounded performance, which is evidenced by the reconstruction of the jagged back of the dragon example, and the generation of more complete surfaces in the remaining examples.

For the *ordinary* dataset, we also sample 5000 points for each shape and add randomized Gaussian noise $\sigma = 0.005$ to the point clouds. This dataset encompasses 486 shapes in various range of types, particularly including numerous thin structures. The qualitative comparisons are depicted in Fig. 6. The example of the second row is a closed manifold with thin structure. Traditional methods smooth out the original thickness. Accordingly, the reconstructed surface by iPSR cannot converge to a satisfactory mesh for the output of these approaches. By contrast, our method takes a global

perspective with the help of the winding number, resulting in superior performance.

We also provide quantitative comparisons in terms of the two-way Chamfer distance (CD) and the symmetric normal consistency (NC) in Table 2 with the ground truth mesh as the reference. The CD value is computed as follows:

$$CD(P, P') = \frac{1}{|P|} \sum_{\mathbf{p}_i \in P} \min_{\mathbf{p}_j \in P'} \|\mathbf{p}_i - \mathbf{p}_j\|_2 + \frac{1}{|P'|} \sum_{\mathbf{p}_j \in P'} \min_{\mathbf{p}_i \in P} \|\mathbf{p}_j - \mathbf{p}_i\|_2, \quad (29)$$

where P and P' are densely sampled point clouds with 10^5 points from the reconstructed mesh and the ground truth mesh, respectively. The normal consistency $NC(A, B)$ is computed as the average absolute normal dot product from the samples in A to its nearest neighbor in the samples of B . The symmetric NC is computed as $0.5 \times (NC(A, B) + NC(B, A))$.

Each row of Table 2 encompasses the corresponding shape of Fig. 6. Additionally, we report the average value across the entire dataset with a total of 486 shapes in the last row. The results demonstrate the superior performance achieved by our method.

Except for the traditional denoising approaches, we compare our method with Shape As Point (SAP) [Peng et al. 2021], which proposes a differentiable Poisson solver for optimization and learning-based methods of surface reconstruction. The main focus of SAP is completely different from our method. The optimization-based method of SAP does not address the noise specifically, as shown in Fig. 5. By contrast, our method optimizes the point positions and generates improved surfaces. The learning-based surface reconstruction of SAP involves a neural network and requires a substantial amount of training data. Therefore, we only conduct comparisons with the optimization-based method of SAP.

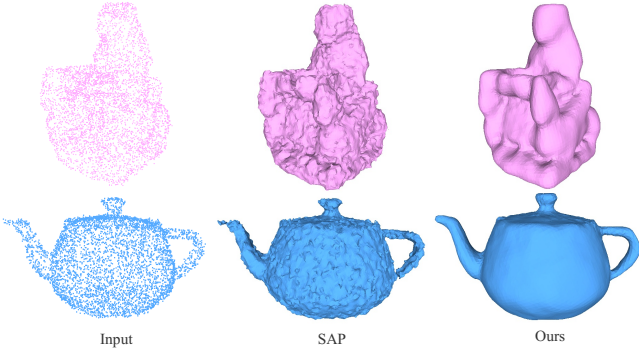


Fig. 5. Qualitative comparisons of our method with the optimization-based SAP method [Peng et al. 2021].

6.3 Results of the Learning-based Method

In this section, we conduct experiments to evaluate the effectiveness of the learning-based method, wherein we incorporate the winding clearness as a geometric constraint to enhance the quality of the generated point clouds. Our baseline is the PVD method [Zhou et al. 2021], which trains a shape generation model on the ShapeNet dataset [Chang et al. 2015]. Each generated point cloud consists of 2048 points. The authors provide several pre-trained models, such as “chair_1799.pth” and “car_3999.pth”, wherein the number represents the trained epoch minus one. We fine-tune these models using the joint training strategy proposed in Section 5.2. The learning rate is set to $2e^{-7}$, and the ρ value in Equation (28) is set to 1.0. The experiments are conducted on a single NVIDIA GeForce RTX 4090 GPU. We train the

chair model for an additional 13 epochs and the car model for 26 epochs. Each training process takes approximately 26 hours.

In addition to the single-category experiment, we test our method for unconditional generation across all 55 classes. Given that the authors do not release the model for generating all 55 classes, we initially trained the models for 400 epochs with a decayed learning rate of 0.995 and keep all other parameters consistent with the source code provided by the authors. We then fine-tune the models for an additional 3 epochs within 46 hours using our method.

The quantitative comparisons are shown in Table 3, where we demonstrate the results for the chair, car category and all the 55 classes. The baseline results are labeled as “PVD” and the results obtained by our method is denoted as “PVD+Ours”. To ensure a fair comparison, we also include the results of “PVD+Ablation”, wherein our method is run with $\rho = 0$ in Equation (28) to exclude the contribution of the winding clearness term. Equal numbers of epochs are used for ablations (13 for chairs, 26 for cars, and 3 for 55 classes). The shapes are generated using the same initial Gaussian prior and intermediate Gaussian noise z . The evaluation metrics include the 1-Nearest Neighbor Accuracy (1-NNA), the winding clearness error (WCE), and the mean absolute distance-to-surface (MADS) between the point cloud and the generated mesh of PGR [Lin et al. 2023], which is introduced in Section 3.

The 1-NNA metric is first introduced in this problem by PointFlow [Yang et al. 2019]. This metric mainly measures the identity degree between two data distributions S_g and S_r . Let $S_{-X} = S_g \cup S_r - X$, and N_X be the nearest neighbor of X in S_X . The 1-NNA value can be computed as follows:

$$1 - \text{NNA}(S_g, S_r) = \frac{\sum_{X \in S_g} \mathbb{I}[N_X \in S_g] + \sum_{Y \in S_r} \mathbb{I}[N_Y \in S_r]}{|S_g| + |S_r|}. \quad (30)$$

We report both the 1-NNA CD (Chamfer distance) and 1-NNA EMD (earth mover distance) using the code provided by PVD. We observe that running the same code on different devices may result in slightly distinct outputs in the generated point sets, causing variations in the 1-NNA values. Accordingly, all reported results are based on the experiments conducted on the same device of our lab. The WCE can be computed by Equations (17) and (16), and the MADS is computed as follows:

$$\text{MADS}(P, P') = \frac{1}{|P|} \sum_{\mathbf{p}_i \in P} \min_{\mathbf{p}_j \in P'} \|\mathbf{p}_i - \mathbf{p}_j\|_2, \quad (31)$$

where P is the generated point cloud and P' is a densely sampled point cloud with 10^5 points from the reconstructed mesh of P .

The 1-NNA metric primarily measures the similarity between the generated and the test datasets. Meanwhile, the WCE and MADS metrics specifically indicate the quality of the generated point clouds, which are our main focus and are emphasized using bold in Table 3. The results indicate that our method significantly improves the quality of the generated point sets while maintaining similarity with the original data distributions.

Fig. 8 displays the qualitative results, which shows the shapes generated within the same initial Gaussian prior and intermediate noises. The only difference is the network parameters. We also colorize the distance from point clouds to the generated surfaces, which further demonstrates the improvement of point cloud quality achieved by our method.

7 LIMITATION AND FUTURE WORK

In this work, we propose winding clearness to represent the clarity of the interior/exterior relationship formed by the winding number field. We outline the formulation for calculating the winding clearness error and utilize it as a loss function for differentiable point cloud optimization. Our method significantly enhances the overall quality of the point cloud by optimizing the point positions to improve the winding clearness.

Table 3. Quantitative comparison of PVD generation with and without the winding clearness constraint. The winding clearness error (WCE) and the mean absolute distance-to-surface (MADS) values are multiplied by 10^3 .

Method	Chair			
	1-NNA CD ↓	1-NNA EMD ↓	WCE ↓	MADS ↓
PVD	0.566	0.569	4.35	5.40
PVD+Ablation	0.575	0.545	4.42	5.58
PVD+Ours	0.574	0.546	<u>3.65</u>	<u>4.28</u>
Method	Car			
	1-NNA CD ↓	1-NNA EMD ↓	WCE ↓	MADS ↓
PVD	0.563	0.524	4.39	7.33
PVD+Ablation	0.581	0.517	4.45	7.45
PVD+Ours	0.601	0.503	<u>3.45</u>	<u>6.18</u>
Method	55 Classes			
	1-NNA CD ↓	1-NNA EMD ↓	WCE ↓	MADS ↓
PVD	0.633	0.600	4.64	6.40
PVD+Ablation	0.607	0.563	4.70	6.55
PVD+Ours	0.614	0.557	<u>3.57</u>	<u>4.65</u>

Nevertheless, our method still has some limitations. The primary drawbacks are the time and memory requirements associated with our current implementation due to the global computation required by the winding number. Processing a point cloud with 5000 points entails approximately 68 s and utilizes 14 GB of memory on a GPU. The operation of $A^T A$ has a time complexity of $O(N^3)$ and a space complexity of $O(N^2)$. However, we believe that we provide a fresh perspective for addressing the thin structure denoising from a global perspective. Decomposing the solving process of the linear system in CG [Hestenes and Stiefel 1952] (without explicitly expressing $A^T A$) may reduce the time complexity to $O(N^2)$. A further solution to this issue is to apply the FMM [Greengard and Rokhlin 1987] similar to fast winding [Barill et al. 2018] and GR [Lu et al. 2019]. The movement of the point positions during the optimization process needs to be taken into account for incorporating FMM. Additionally, our method lacks a feature preserving mechanism. A potential solution involves detecting sharp features before optimization and assigning higher weights to the feature points in Equation (18). Furthermore, we can observe from Fig. 1 that the degree to which the winding number field exceeds 0.5 within the surface becomes less significant for large noise. Encouraging more “1” values when solving Equation (14) may improve the effectiveness of our method.

REFERENCES

Alexander Agathos, Philip N. Azariadis, and Sofia Kyratzi. 2022. Elliptic Gabriel Taubin smoothing of point clouds. *Comput. Graph.* 106 (2022), 20–32.

Haim Avron, Andrei Sharf, Chen Greif, and Daniel Cohen-Or. 2010. l_1 -Sparse reconstruction of sharp point set surfaces. *ACM Trans. Graph.* 29, 5 (2010), 135:1–135:12.

Gavin Barill, Neil G. Dickson, Ryan M. Schmidt, David I. W. Levin, and Alec Jacobson. 2018. Fast winding numbers for soups and clouds. *ACM Trans. Graph.* 37, 4 (2018), 43.

Matthew Berger, Andrea Tagliasacchi, Lee M. Seversky, Pierre Alliez, Gaël Guennebaud, Joshua A. Levine, Andrei Sharf, and Cláudio T. Silva. 2017. A Survey of Surface Reconstruction from Point Clouds. *Comput. Graph. Forum* 36, 1 (2017), 301–329.

Frédéric Cazals and Marc Pouget. 2005. Estimating differential quantities using polynomial fitting of osculating jets. *Comput. Aided Geom. Des.* 22 (2005), 121–146.

Angel X. Chang, Thomas A. Funkhouser, Leonidas J. Guibas, Pat Hanrahan, Qi-Xing Huang, Zimo Li, Silvio Savarese, Manolis Savva, Shuran Song, Hao Su, Jianxiong Xiao, Li Yi, and Fisher Yu. 2015. ShapeNet: An Information-Rich 3D Model Repository. *CoRR abs/1512.03012* (2015). arXiv:1512.03012 <http://arxiv.org/abs/1512.03012>

Dawson Haggerty et al. 2021. *trimesh 3.9*. <https://trimesh.org/>

Julie Digne and Carlo de Franchis. 2017. The Bilateral Filter for Point Clouds. *Image Process. Line* 7 (2017), 278–287.

Andreas Fabri and Sylvain Pion. 2009. CGAL: the Computational Geometry Algorithms Library. In *17th ACM SIGSPATIAL International Symposium on Advances in*

Geographic Information Systems. ACM, 538–539.

L. Greengard and V. Rokhlin. 1987. A fast algorithm for particle simulations. *J. Comput. Phys.* 73, 2 (1987), 325–348.

Gaël Guennebaud and Markus H. Gross. 2007. Algebraic point set surfaces. *ACM Trans. Graph.* 26, 3 (2007), 23.

Xian-Feng Han, Jesse S. Jin, Ming-Jie Wang, Wei Jiang, Lei Gao, and Liping Xiao. 2017. A review of algorithms for filtering the 3D point cloud. *Signal Process. Image Commun.* 57 (2017), 103–112.

M. R. Hestenes and E. L. Stiefel. 1952. Methods of conjugate gradients for solving linear systems. *Journal of Research of the National Bureau of Standards (United States)* 49 (1952).

Jonathan Ho, Ajay Jain, and Pieter Abbeel. 2020a. Denoising Diffusion Probabilistic Models. In *Advances in Neural Information Processing Systems 33: Annual Conference on Neural Information Processing Systems 2020, NeurIPS 2020, December 6–12, 2020, virtual*.

Jonathan Ho, Ajay Jain, and Pieter Abbeel. 2020b. Denoising Diffusion Probabilistic Models. In *Annual Conference on Neural Information Processing Systems*.

Fei Hou, Chiyu Wang, Wencheng Wang, Hong Qin, Chen Qian, and Ying He. 2022. Iterative poisson surface reconstruction (iPSR) for unoriented points. *ACM Trans. Graph.* 41, 4 (2022), 128:1–128:13.

Hui Huang, Dan Li, Hao Zhang, Uri M. Ascher, and Daniel Cohen-Or. 2009. Consolidation of unorganized point clouds for surface reconstruction. *ACM Trans. Graph.* 28, 5 (2009), 176.

Hui Huang, Shihao Wu, Minglun Gong, Daniel Cohen-Or, Uri M. Ascher, and Hao (Richard) Zhang. 2013. Edge-aware point set resampling. *ACM Trans. Graph.* 32, 1 (2013), 9:1–9:12.

Zhangjin Huang, Yuxin Wen, Zihao Wang, Jinjuan Ren, and Kui Jia. 2022. Surface Reconstruction from Point Clouds: A Survey and a Benchmark. *CoRR abs/2205.02413* (2022). arXiv:2205.02413

Alec Jacobson, Ladislav Kavan, and Olga Sorkine-Hornung. 2013. Robust inside-outside segmentation using generalized winding numbers. *ACM Trans. Graph.* 32, 4 (2013), 33:1–33:12.

Diederik P. Kingma and Jimmy Ba. 2015. Adam: A Method for Stochastic Optimization. In *3rd International Conference on Learning Representations, Yoshua Bengio and Yann LeCun (Eds.)*.

Sebastian Koch, Albert Matveev, Zhongshi Jiang, Francis Williams, Alexey Artemov, Evgeny Burnaev, Marc Alexa, Denis Zorin, and Daniele Panozzo. 2019. ABC: A Big CAD Model Dataset for Geometric Deep Learning. In *Proceedings of the IEEE/CVF Conference on Computer Vision and Pattern Recognition (CVPR)*.

Siyu Lin, Dong Xiao, Zuoqiang Shi, and Bin Wang. 2023. Surface Reconstruction from Point Clouds without Normals by Parametrizing the Gauss Formula. *ACM Trans. Graph.* 42, 2 (2023), 14:1–14:19.

Yaron Lipman, Daniel Cohen-Or, David Levin, and Hillel Tal-Ezer. 2007. Parameterization-free projection for geometry reconstruction. *ACM Trans. Graph.* 26, 3 (2007), 22.

Zhijian Liu, Haotian Tang, Yujun Lin, and Song Han. 2019. Point-Voxel CNN for Efficient 3D Deep Learning. In *Annual Conference on Neural Information Processing Systems*. 963–973.

Wenjia Lu, Zuoqiang Shi, Jian Sun, and Bin Wang. 2019. Surface Reconstruction Based on the Modified Gauss Formula. *ACM Trans. Graph.* 38, 1 (2019), 2:1–2:18.

Xuequan Lu, Scott Schaefer, Jun Luo, Lizhuang Ma, and Ying He. 2022. Low Rank Matrix Approximation for 3D Geometry Filtering. *IEEE Trans. Vis. Comput. Graph.* 28, 4 (2022), 1835–1847. <https://doi.org/10.1109/TVCG.2020.3026785>

Shitong Luo and Wei Hu. 2021. Diffusion Probabilistic Models for 3D Point Cloud Generation. In *IEEE Conference on Computer Vision and Pattern Recognition*. Computer Vision Foundation / IEEE, 2837–2845.

Gal Metzer, Rana Hanocka, Denis Zorin, Raja Giryes, Daniele Panozzo, and Daniel Cohen-Or. 2021. Orienting point clouds with dipole propagation. *ACM Trans. Graph.* 40, 4 (2021), 165:1–165:14.

Oliver, L. et al. 2012. Three D Scans: Free 3D scan archive. <https://threedscans.com>

A. Cengiz Öztireli, Gaël Guennebaud, and Markus H. Gross. 2009. Feature Preserving Point Set Surfaces based on Non-Linear Kernel Regression. *Comput. Graph. Forum* 28, 2 (2009), 493–501.

Adam Paszke, Sam Gross, Francisco Massa, Adam Lerer, James Bradbury, Gregory Chanan, Trevor Killeen, Zeming Lin, Natalia Gimelshein, Luca Antiga, Alban Desmaison, Andreas Köpf, Edward Z. Yang, Zach DeVito, Martin Raison, Alykhan Tejani, Sasank Chilamkurthy, Benoit Steiner, Lu Fang, Junjie Bai, and Soumith Chintala. 2019. PyTorch: An Imperative Style, High-Performance Deep Learning Library. *CoRR abs/1912.01703* (2019). arXiv:1912.01703 <http://arxiv.org/abs/1912.01703>

Songyou Peng, Chiyu Jiang, Yiyi Liao, Michael Niemeyer, Marc Pollefeys, and Andreas Geiger. 2021. Shape As Points: A Differentiable Poisson Solver. In *Annual Conference on Neural Information Processing Systems*. 13032–13044.

Hanspeter Pfister, Matthias Zwicker, Jeroen van Baar, and Markus Gross. 2000. Surfels: Surface Elements as Rendering Primitives (*SIGGRAPH '00*). ACM Press/Addison-Wesley Publishing Co., USA, 335–342.

- Marie-Julie Rakotosaona, Vittorio La Barbera, Paul Guerrero, Niloy J. Mitra, and Maks Ovsjanikov. 2020. PointCleanNet: learning to Denoise and Remove Outliers from Dense Point Clouds. *Comput. Graph. Forum* 39, 1 (2020), 185–203.
- Yujing Sun, Scott Schaefer, and Wenping Wang. 2015. Denoising point sets via L_0 minimization. *Comput. Aided Geom. Des.* 35–36 (2015), 2–15.
- Ningna Wang, Bin Wang, Wenping Wang, and Xiaohu Guo. 2022a. Computing Medial Axis Transform with Feature Preservation via Restricted Power Diagram. *ACM Trans. Graph.* 41, 6 (2022), 188:1–188:18.
- Pengfei Wang, Zixiong Wang, Shiqing Xin, Xifeng Gao, Wenping Wang, and Changhe Tu. 2022b. Restricted Delaunay Triangulation for Explicit Surface Reconstruction. *ACM Trans. Graph.* 41, 5 (2022), 180:1–180:20.
- W. L. Wendland. 2009. *On the Double Layer Potential*. Birkhäuser Basel.
- Walter Wohlkinger, Aitor Aldoma, Radu Bogdan Rusu, and Markus Vincze. 2012. 3DNet: Large-scale object class recognition from CAD models. In *IEEE International Conference on Robotics and Automation*. IEEE, 5384–5391.
- Rui Xu, Zhiyang Dou, Ningna Wang, Shiqing Xin, Shuang-Min Chen, Mingyan Jiang, Xiaohu Guo, Wenping Wang, and Changhe Tu. 2023. Globally Consistent Normal Orientation for Point Clouds by Regularizing the Winding-Number Field. *ACM Trans. Graph.* 42, 4 (2023), 111:1–111:15.
- Guandao Yang, Xun Huang, Zekun Hao, Ming-Yu Liu, Serge J. Belongie, and Bharath Hariharan. 2019. PointFlow: 3D Point Cloud Generation With Continuous Normalizing Flows. In *IEEE/CVF International Conference on Computer Vision*. IEEE, 4540–4549.
- Xiaohui Zeng, Arash Vahdat, Francis Williams, Zan Gojcic, Or Litany, Sanja Fidler, and Karsten Kreis. 2022. LION: Latent Point Diffusion Models for 3D Shape Generation. In *NeurIPS*.
- Dongbo Zhang, Xuequan Lu, Hong Qin, and Ying He. 2021. Pointfilter: point Cloud Filtering via Encoder-Decoder Modeling. *IEEE Trans. Vis. Comput. Graph.* 27, 3 (2021), 2015–2027.
- Feng Zhang, Chao Zhang, Huamin Yang, and Lin Zhao. 2019. Point Cloud Denoising with Principal Component Analysis and a Novel Bilateral Filter. *Traitement du Signal* 36, 5 (2019), 393–398.
- Linqi Zhou, Yilun Du, and Jiajun Wu. 2021. 3D Shape Generation and Completion through Point-Voxel Diffusion. In *2021 IEEE/CVF International Conference on Computer Vision*. IEEE, 5806–5815.
- Lang Zhou, Guoxing Sun, Yong Li, Weiqing Li, and Zhiyong Su. 2022. Point cloud denoising review: from classical to deep learning-based approaches. *Graph. Model.* 121 (2022), 101140.
- Qingnan Zhou, Eitan Grinspun, Denis Zorin, and Alec Jacobson. 2016. Mesh arrangements for solid geometry. *ACM Trans. Graph.* 35, 4 (2016), 39:1–39:15.
- Qingnan Zhou and Alec Jacobson. 2016. Thingi10K: A Dataset of 10, 000 3D-Printing Models. *CoRR* abs/1605.04797 (2016). arXiv:1605.04797

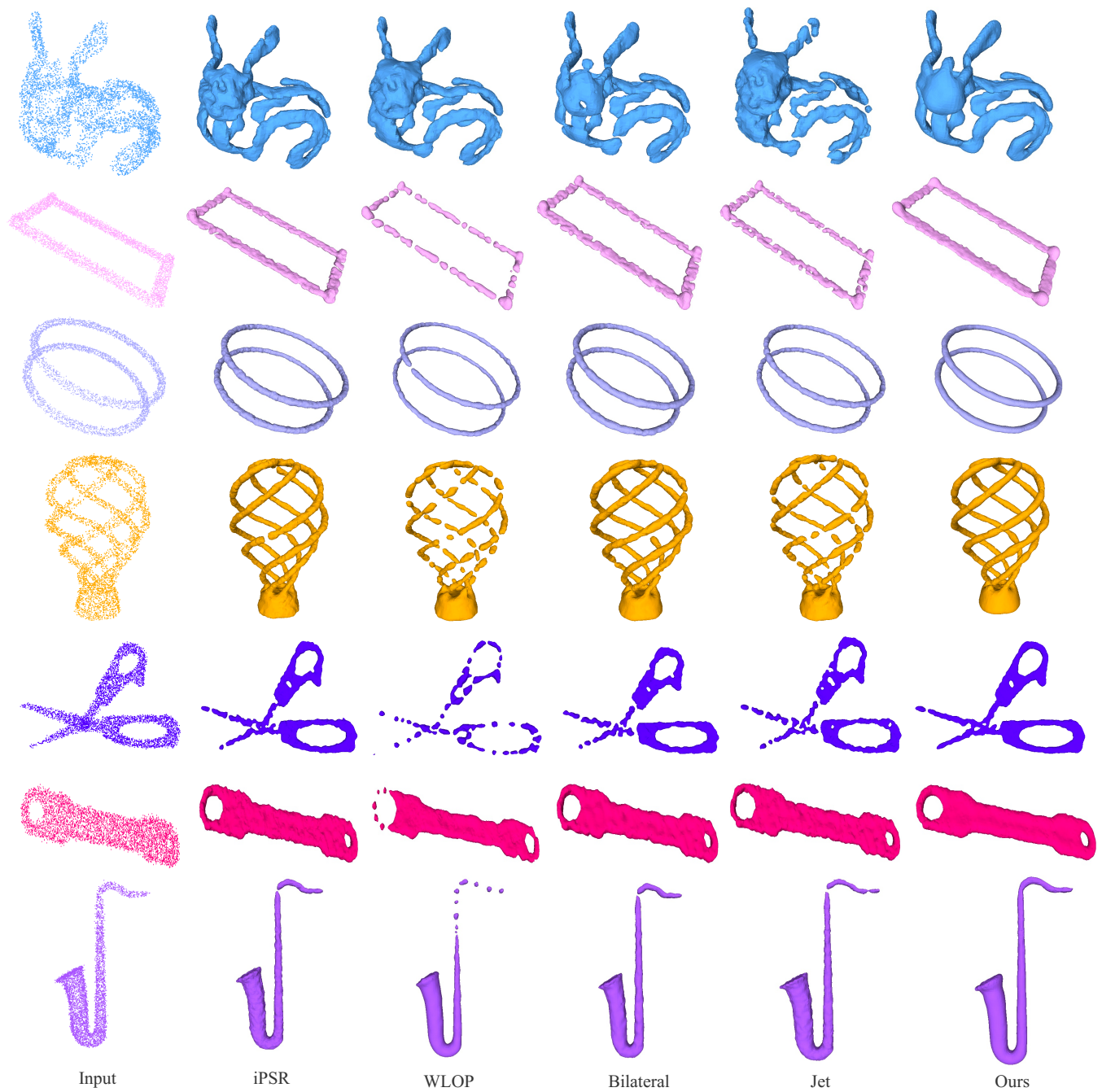


Fig. 6. Qualitative comparisons on the ordinary dataset. Our method exhibits superior performance against local feature-based methods.

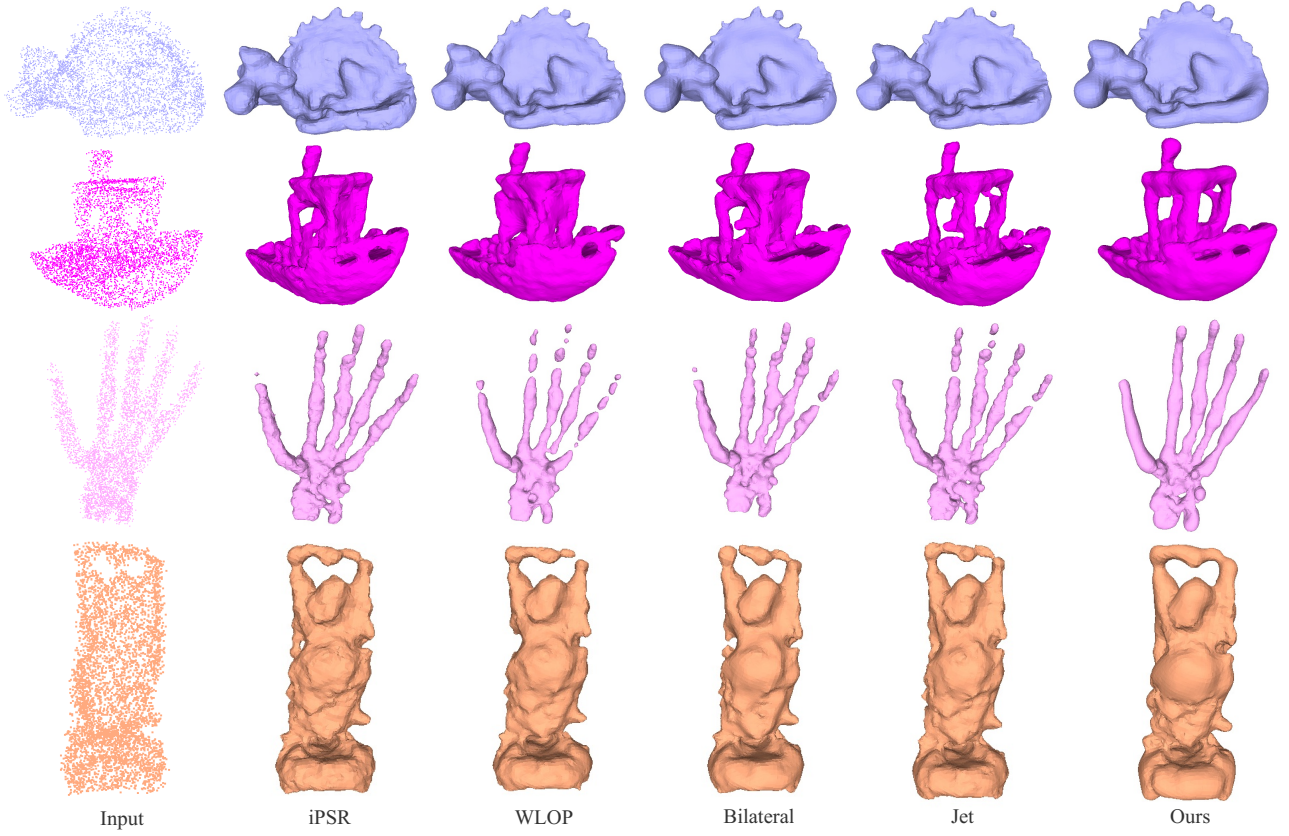


Fig. 7. Qualitative comparisons on several commonly used geometric shapes. Our method achieves well-rounded performance.

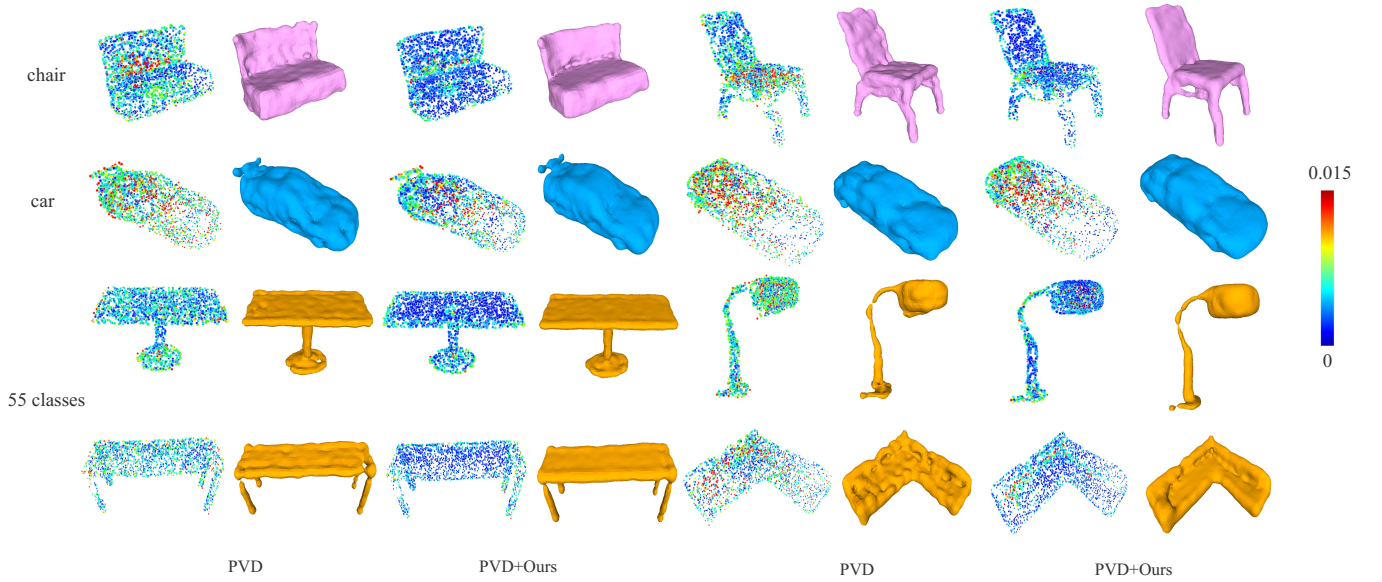


Fig. 8. Qualitative comparisons of PVD generation with and without fine-tuning by the winding clearness constraint. Our method significantly improves the quality of the generated point sets.

Supplementary Material

A THE IMPORTANCE OF THE REGULARIZATION TERM $R(P)$

In this section, we aim to explicate the significance of the regularization term $R(P)$ in Equation (14) of the original manuscript. An alternative approach for computing the surfels μ in Section 4 is concatenating the matrix $A_1(P)$ of point constraints and $A_2(P)$ of boundary constraints, and obtain a square matrix $C(P)$ as follows:

$$C(P) = (A_1^T(P), A_2^T(P))^T. \quad (1)$$

Additionally, we define $c = (1/2, 1/2, \dots, 0, 0, \dots, 0)^T$ as a vector with the first N values to $1/2$, and the remaining values to 0. Subsequently, the surfels μ can be solved by the following equation:

$$C(P)\mu = c. \quad (2)$$

If $C(P)$ is invertible, the surfels μ can be computed as $\mu = C^{-1}(P)c$. In this case, the winding clearness error will always be zero. However, it becomes challenging to generate a smooth and reliable winding number field without including the regularization term $R(P)$, which controls the magnitude of μ . If the solution of Equation (2) yields high magnitudes for μ , it contradicts the meaning of the surfel. In this case, the generated function cannot represent the winding number field of this point cloud, i.e., 1 inside and 0 outside. This phenomenon is demonstrated in Fig. 1, where we show the implicit field generated by a 2D circle of $\sigma = 0.001$ with (a) and without (b) the regularization term $R(P)$. We can observe in Fig. 1 (b) that the function becomes jagged and unreliable if we solve Equation (2) directly. Fig. 1 (a) illustrates the results of incorporating the regularization term $R(P)$ in the formulation, which highlights the necessity of $R(P)$ in creating a viable winding number field. If Equation (2) above is also regularized and formulated as a least squares problem, it shares similarities with the formulation in the original manuscript.

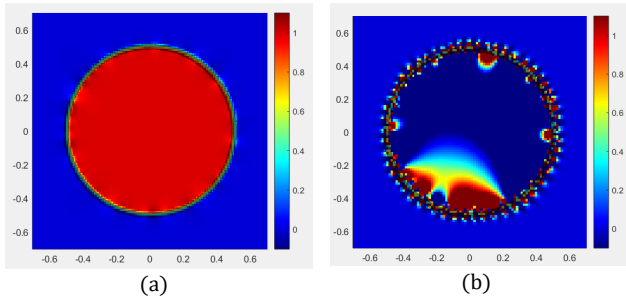


Fig. 1. Winding number field formed by a 2D circle of $\sigma = 0.001$ with (a) and without (b) the regularization term $R(P)$.

Author's address:

© 2024

B COMPARISONS WITH THE POINT PROJECTION METHOD

Our method aims to optimize the point positions for improving the winding clearness of the input point set. Both the input and output of our method are point clouds. In the original manuscript, the reconstruction method utilized in Section 6.2 serve as a way to showcase the quality of the denoised point clouds. However, an alternative approach for generating denoised point clouds involves applying an unoriented surface reconstruction method with a noise-adaptive parameter, followed by sampling or projecting the noisy point clouds onto the generated surface. We will illustrate the distinctions between our method and the projection-based method from three perspectives:

Firstly, surface reconstruction involves extracting the iso-surface from the implicit field. In cases where the computation fails to achieve consistent normal orientation or encounters difficulties with thin or complex features, the resulting surface may have missing structures compared to the original point cloud. When the noisy point cloud is projected onto the reconstructed surface, it also lead to missing regions in the results. In contrast, our method directly optimizes the point positions, effectively addressing this issue. Figure 2 provides a visual comparison between our method and the projection method. The surface is reconstructed using PGR [Lin et al. 2022] with a noise-adaptive parameter setting. The projected points are marked as “PGR Proj.” in this figure. From the first example, it can be observed that the projected point cloud loses details in thin structures due to incomplete reconstruction of the surface. Our method efficiently handles this situation. In the second example, the reconstructed surface not only exhibits missing features but also undergoes overall shrinkage comparing to the original point cloud. Therefore, the projected point cloud cannot accurately express the shape of the input.

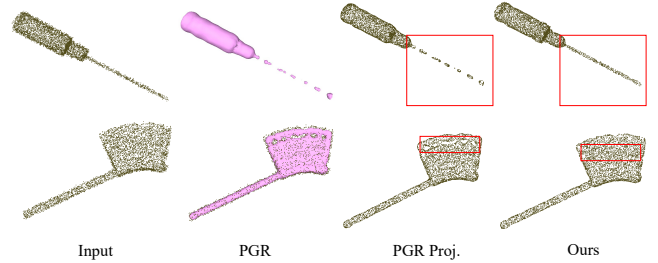


Fig. 2. Qualitative comparisons of our method with the point projection method. The surface is reconstructed by PGR with a noise-adaptive parameter setting.

Secondly, the denoised point clouds of our method lead to more complete surface reconstruction results compared with the original point clouds in many cases. This advantage has been demonstrated in Fig. 6 of the original manuscript, where iPSR [Hou et al. 2022] is utilized for surface reconstruction. We also provide results on PGR in Fig. 3 below to further illustrate this advantage.

Lastly, our approach introduces a differentiable point cloud optimization scheme that can be extended to the learning-based point processing, such as the diffusion-based generative model outlined in Section 5.2. Taking an alternative perspective, we extend PGR to a fully differentiable point-based form. The results presented in Section 6.3 also showcase the enhancements achieved by our method in both the point clouds and the reconstructed surfaces.

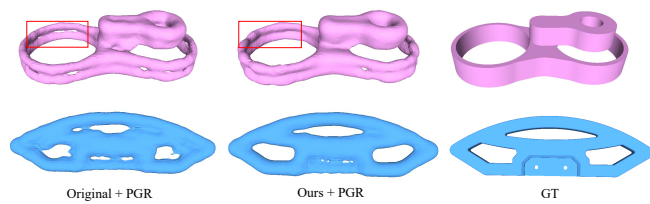


Fig. 3. Reconstruction of PGR (with a noise adaptive parameter setting) using the original input and the optimized point clouds from our method.

REFERENCES

- Fei Hou, Chiyu Wang, Wencheng Wang, Hong Qin, Chen Qian, and Ying He. 2022. Iterative poisson surface reconstruction (iPSR) for unoriented points. *ACM Trans. Graph.* 41, 4 (2022), 128:1–128:13. <https://doi.org/10.1145/3528223.3530096>
- Siyu Lin, Dong Xiao, Zuoqiang Shi, and Bin Wang. 2022. Surface Reconstruction from Point Clouds without Normals by Parametrizing the Gauss Formula. *ACM Transactions on Graphics* 42, 2 (2022), 14:1–14:19.